

1 **Cell segmentation-free inference of cell types from *in situ* transcriptomics data**

2

3 **Author names**

4 Jeongbin Park^{1,2,3,†}, Wonyl Choi^{4,†}, Sebastian Tiesmeyer¹, Brian Long⁵, Lars E. Borm⁶, Emma
5 Garren⁵, Thuc Nghi Nguyen⁵, Bosiljka Tasic⁵, Simone Codeluppi^{6,7}, Tobias Graf¹, Matthias
6 Schlesner⁸, Oliver Stegle^{3,9}, Roland Eils^{1,10,†,*} & Naveed Ishaque^{1,†,*}

7

8 **Affiliations**

9 ¹Digital Health Center, Berlin Institute of Health (BIH) and Charité Universitätsmedizin, Berlin,
10 Germany;

11 ²Faculty of Biosciences, Heidelberg University, Heidelberg, Germany;

12 ³Division of Computational Genomics and System Genetics, German Cancer Research Center
13 (DKFZ), Heidelberg, Germany;

14 ⁴Department of Computer Science, Boston University, Boston, the United States of America;

15 ⁵Allen Institute for Brain Science, Seattle, WA, USA;

16 ⁶Division of molecular neurobiology, Department of medical biochemistry and biophysics,
17 Karolinska Institutet, Stockholm, Sweden;

18 ⁷Science for life laboratory, Stockholm, Sweden;

19 ⁸Bioinformatics and Omics Data Analytics, German Cancer Research Center (DKFZ),
20 Heidelberg, Germany;

21 ⁹Genome Biology Unit, European Molecular Biology Laboratory (EMBL), Heidelberg, Germany;

22 ¹⁰Health Data Science Unit, Heidelberg University Hospital, Heidelberg, Germany;

23

24 **Author List Footnotes**

25 † These authors contributed equally to this work.

26 ‡These authors jointly supervised the work.

27

28 **Contact information**

29 *Correspondence: Roland Eils (roland.eils@charite.de) and Naveed Ishaque

30 (naveed.ishaque@charite.de)

31 **Abstract**

32 Multiplexed fluorescence *in situ* hybridization techniques have enabled cell-type identification,
33 linking transcriptional heterogeneity with spatial heterogeneity of cells. However, inaccurate cell
34 segmentation reduces the efficacy of cell-type identification and tissue characterization. Here,
35 we present a novel method called Spot-based Spatial cell-type Analysis by Multidimensional
36 mRNA density estimation (SSAM), a robust cell segmentation-free computational framework for
37 identifying cell-types and tissue domains in 2D and 3D. SSAM is applicable to a variety of *in*
38 *situ* transcriptomics techniques and capable of integrating prior knowledge of cell types. We
39 apply SSAM to three mouse brain tissue images: the somatosensory cortex imaged by
40 osmFISH, the hypothalamic preoptic region by MERFISH, and the visual cortex by multiplexed
41 smFISH. We found that SSAM detects regions occupied by known cell types that were
42 previously missed and discovers new cell types.

43
44 **Keywords**

45 *In situ* transcriptomics, spatial cell-type calling, cell segmentation-free, multiplexed FISH, SSAM,
46 osmFISH, mFISH, multiplexed smFISH, MERFISH, spatially resolved RNA profiling

47 Introduction

48 The underlying transcriptional and spatial heterogeneity of cells gives rise to the plethora of
49 phenotypes observed in cell types, tissues, organs, and organisms. Recent technological
50 advances¹ have seen the profound adoption of single-cell sequencing to unravel transcriptional
51 heterogeneity in healthy and diseased tissues, and have subsequently given rise to international
52 consortia such as the Human Cell Atlas (HCA)². Such efforts would not be possible without
53 computational frameworks supporting the analysis of single-cell sequencing data³. Linking this
54 transcriptional heterogeneity with spatial heterogeneity of cells is a critical factor in
55 understanding cell identity in the context of the tissue, for example, revealing the transcriptional
56 basis of invasive cancer regions⁴ and highlighting the rich diversity of neuronal subtype
57 expression and localization⁵. Recently developed multiplexed fluorescence in-situ hybridization⁶⁻
58 ⁸ and *in situ* mRNA tissue sequencing techniques⁹⁻¹⁴ have enabled the simultaneous
59 measurement of multiple mRNAs in a spatial context.

60
61 Traditionally, mRNA molecules identified by *in situ* transcriptomics are assigned to cells and
62 subsequently used for computing gene expression profiles of those cells¹⁵⁻¹⁸. Identification of
63 cells relies on cell segmentation, a procedure demarcating the interior and exterior of the cell
64 membranes, which relies on additional signals or landmarks obtained by staining nuclei¹⁹, cell
65 membrane²⁰⁻²², or total poly-A RNA^{5,6}. However, accurate cell segmentation is difficult to
66 achieve with current techniques due to tightly apposed or overlapping cells, uneven cell borders,
67 varying cell and nuclear shapes, signal intensity variation, probe fluorescence emission
68 efficiency variation, and tiling artifacts²³. Such obstacles can result in detecting fewer cells or
69 incorrect cell borders. Subsequent analysis would then be spatially restricted to inaccurately
70 segmented cells and may mean that large portions of meaningful mRNA signals are discarded.
71 This may result in incorrect cell-type signatures, incomplete cell-type maps, or missing rare cell
72 types. Therefore, there is a need for robust cell segmentation-independent methods for

73 identifying cell-type signatures, cell-type organization, and tissue domains from
74 multidimensional mRNA expression data in complex tissues. These methods could be used for
75 datasets lacking landmarks or to validate segmentation-based approaches.

76
77 Here we introduce a novel computational framework named Spot-based Spatial cell-type
78 Analysis by Multidimensional mRNA density estimation (SSAM). In contrast to existing methods,
79 SSAM departs from the spatial restriction of approaches based on cell segmentation and
80 instead identifies cell types using mRNA signals in the image, without the need for prior cell
81 segmentation. Furthermore, instead of labelling only segmented regions, our approach assigns
82 cell-type labels to each pixel, ensuring a more complete picture of cell-type specific spatial
83 heterogeneity.

84
85 We apply SSAM to three mouse brain tissue images obtained by different techniques: the
86 somatosensory cortex (SSp) by osmFISH, the hypothalamic preoptic region (POA) by
87 MERFISH, and the visual cortex (VISp) by multiplexed smFISH. With all three datasets, we
88 demonstrate the robustness of SSAM in identifying 1) cell types *in situ*, 2) spatial distribution of
89 cell types, 3) spatial relationships between cell types, and 4) tissue domains (e.g., cortical layers)
90 based on the local composition of cell types without fine-tuning of parameters. We demonstrate
91 that SSAM 1) correctly identifies the spatial distribution of known cell types in regions missed in
92 the SSp by cell segmentation based methods for the osmFISH data ; 2) can analyze the POA
93 MERFISH 3D data using the same parameters as for the 2D SSp osmFISH data without any
94 extra adjustments of the settings; 3) identifies new and rare cell types in the VISp, multiplexed
95 smFISH data.

96

97 **Results**

98 **The SSAM computational framework**

99 SSAM consists of 4 major steps (**Fig. 1**), namely 1) mRNA signal estimation and downsampling;
100 2) computation of cell-type signatures; 3) generation of a cell-type map; and 4) identification of
101 tissue domains.

102

103 In the first step, SSAM estimates mRNA signal intensity over the tissue image (**Fig. 1A**). Firstly,
104 for each gene, mRNA signal intensity distribution is estimated by applying a Kernel Density
105 Estimation (KDE) with a Gaussian kernel, which is then resolved to pixels in the image. The
106 mRNA signal intensity distribution for each gene is stacked to create a gene expression vector
107 field, which is a multichannel image where the pixels encode the expected density of mRNA
108 count for each gene. This essentially assigns gene expression profiles to pixels in the image.

109

110 In the second step, SSAM identifies cell-type gene expression signatures by clustering (**Fig. 1B**).
111 Before running the clustering algorithm, SSAM downsamples gene expression vectors to reduce
112 computational processing time. As default, SSAM performs informed downsampling by selecting
113 pixels that are local maxima in the gene vector field (Methods). After that, both the
114 downsampled vectors and the gene expression vector field are normalized (Methods). SSAM
115 clusters the sampled vectors using either DBSCAN²⁴, HDBSCAN²⁵, OPTICS²⁶, or the Louvain
116 community detection method implemented in Seurat²⁷ (Methods). The Louvain method is the
117 default as it has been widely utilized to analyze single cell data. After the clustering step,
118 sampled vectors with a large distance in gene expression space to their cluster medoid are
119 removed as outliers to ensure the quality of selected vectors (**Supplementary Fig. 1B**). The
120 gene expression cluster centroids are used to represent the gene expression signature of a cell
121 type.

122

123 In the third step, SSAM classifies each pixel in the image to create a “cell-type map” (**Fig. 1C**,
124 **Supplementary Fig. 2A**). SSAM includes a guided mode, which assigns pixels to a labeled set
125 of given gene expression signatures (e.g. from scRNA-seq/segmentation), as well as a *de novo*
126 mode, which assigns pixels to the cell type signatures obtained in the previous clustering step.
127 For the classification of pixels, SSAM first creates signature prototypes by averaging the
128 signatures per cell-type class of the given signatures, then it classifies all spots in the vector
129 field according to the maximum correlation to any of the signature prototypes.

130

131 In the fourth step, SSAM identifies tissue domains that have distinct cell-type composition (**Fig.**
132 **1D**). SSAM computes the cell-type compositions in a circular (or spherical) sliding window over
133 the cell-type map and clusters the cell-type composition of each window using agglomerative
134 hierarchical clustering (**Supplementary Fig. 2B**). The resultant clusters represent putative
135 tissue domains. Clusters with high mutual correlation are then merged into a single tissue
136 domain signature, and the cell-type composition of each domain is calculated.

137

138 In the following sections we apply SSAM to three multiplexed FISH datasets obtained using
139 different techniques. We reanalyze two previously published datasets, profiled by osmFISH⁶ and
140 MERFISH⁵, to demonstrate SSAM's strength in comparison to earlier methods. For a newly
141 generated multiplexed smFISH dataset we demonstrate that SSAM can unravel novel biological
142 insights into the spatial cellular organization of the brain.

143

144 **SSAM improves astrocyte and ventricle detection in the mouse brain somatosensory** 145 **cortex (SSp)**

146 To demonstrate the utility of SSAM, we analyzed published osmFISH data, where the
147 transcripts of 33 cell-type marker genes were localized in 2D space of the mouse brain
148 somatosensory cortex (SSp)⁶ (**Fig. 2, 3, Supplementary Fig. 3, 4**). We compare results

149 obtained from SSAM against the results obtained from Poly-A segmentation from the original
150 study.

151

152 The osmFISH dataset was first analyzed using the guided mode of SSAM. Cell-type maps were
153 generated using cell-type signatures from the prior segmentation-based approach⁶ and another
154 from scRNA-seq^{28,29} (**Supplementary Fig. 4E**).

155

156 To quantify the similarity between the prior segmentation and the cell-type maps generated by
157 SSAM, we calculated a “matching score” for each cell type (Methods). The matching scores
158 between the segmentation from the previous study and SSAM guided by both segmentation-
159 based and scRNA-seq cell-type signatures were generally high (mean and median matching
160 score of 0.67 and 0.78 for segmentation-based, 0.60 and 0.70 for scRNA-seq-based signatures,
161 respectively), indicating a strong agreement of the two cell-type maps as visually apparent
162 (**Supplementary Table 1, 2, Supplementary Fig. 5, 6**).

163

164 Next, we continued with completely *de novo* cell-type identification. The resulting 30 cell-type
165 signatures (**Fig. 2A, B, Supplementary Fig. 7-10**) were consistent with those identified in the
166 segmentation-based clustering and scRNA-seq based cell-type signatures⁶ (**Supplementary**
167 **Fig. 4C, D**), implicating the robustness of the *de novo* cell-type calling by SSAM. Each of the
168 SSAM *de novo* cell-type signature clusters were assigned the label of the closest correlating
169 segmentation-based cluster.

170

171 As with the guided mode analysis, we limit the comparison to the most comparable cell types,
172 excluding cell types with low correlation in gene expression signatures (< 0.8) (**Supplementary**
173 **Table 3, Supplementary Fig. 11**). The matching score result showed high average values
174 (mean and median of 0.76 and 0.83, respectively) and 81% of cell types had a matching score

175 of greater than 0.6. Comparing marker gene expression of cell types having lowest matching
176 score (< 0.3) (**Supplementary Table 3**) confirmed that the SSAM guided cell-type map is in
177 better agreement to their marker gene expression (**Supplementary Fig. 12-13**). Given the low
178 correlation of C. Plexus cell type to the corresponding osmFISH cluster, which is one of the
179 dominant cell types in the ventricle region, high-resolution investigation of Poly-A and DAPI
180 signals confirm the existence of both cell types in the ventricle area (**Fig. 2D**). Since ependymal
181 and choroid plexus cells were small and tightly packed and exhibit relatively lower DAPI and
182 poly-A signal, we concluded that the performance of the watershed algorithm was insufficient to
183 identify cells in the area. Furthermore, we statistically evaluated this for each cell type by
184 comparing the gene expression in the unique parts of the segmentation and SSAM *de novo* cell-
185 type map, to the overlapping parts (Methods). Gene expression of the unique part of SSAM *de*
186 *novo* cell-type map showed higher correlation to the overlapping regions compared to the
187 unique parts of the segmentation (**Supplementary Fig. 14**).

188

189 We then performed domain analysis on the SSAM *de novo* cell-type map. Identified domains
190 correlated well with the known cerebral cortex layers, consistent with results reported in the
191 previous study (**Fig. 3A**). Laminal distribution of cell types is established³⁰, and can be
192 considered as a ground truth for validating the cell type map. Cell-type assignments of
193 excitatory pyramidal cells in the cortical layers conformed closely to known localizations
194 (**Supplementary Fig. 15**). The domains identified as: layer 2/3 primarily consists of Pyramidal
195 L2-3/L5, L2-3, and L3-4 cell types; layer 4 consists of Pyramidal L4 and L3-4 cell types; layer 5
196 consists of Pyramidal L3-5 and L5 cell types; and layer 6 consists of Pyramidal L6 cell types.

197

198 In addition, cell-type composition of the domains revealed that *Mfge8* expressing astrocytes
199 (Astrocyte *Mfge8*) contributed 7-14 % of each of the tissue layers (**Fig. 3B**), in contrast to the

200 significantly fewer numbers of Astrocyte *Mfge8* cells called in the previous study⁶. Comparison
201 of high-resolution images of DAPI and poly-A signals with *Mfge8* expression densities implicates
202 that the poly-A signal was not strong enough to discriminate the presence of astrocyte *Mfge8*
203 cells from the background, while the DAPI images clearly supported the existence of *Mfge8*
204 expressing astrocytes at positions identified by SSAM (**Fig. 2E**). The clear DAPI signal but low
205 poly-A signal for these astrocytes *Mfge8* suggested that they have a lower mRNA content
206 compared to other cells. We compared the total counts of mRNA molecules of astrocytes and
207 other cell types from mouse brain scRNA-seq data³¹ and found that astrocytes exhibited
208 significantly less mRNA molecules than other cell classes (**Supplementary Fig. 4B**). Our
209 observation reveals the inadequacy of the watershed segmentation algorithm applied to poly-A
210 signal when not considering cells with a low total mRNA content. This implies that the original
211 segmentation of these cell types could be less accurate than the SSAM *de novo* cell-type map,
212 therefore also reducing the matching score for these cell types.

213

214 **SSAM confirms diversity of inhibitory and excitatory neuron cell types and their** 215 **localization in the hypothalamic preoptic region (POA) in 3D**

216 To demonstrate the performance of SSAM for three-dimensional *in situ* transcriptomics data, we
217 applied SSAM to previously published MERFISH data, where 135 transcripts were localized in
218 3D space of the hypothalamic preoptic region (POA) of a mouse brain⁵ (**Fig. 4, Supplementary**
219 **Fig. 16, 18**). We compare results obtained from SSAM against the results obtained from DAPI
220 segmentation from the original study.

221

222 We applied both SSAM guided mode and *de novo* mode. For guided mode, the previously
223 known cell-type signatures obtained by segmentation and scRNA-seq were used. For both
224 guided and *de novo* modes, SSAM analysis was performed in 3D space, generating a 3D cell-
225 type map (**Fig. 4B**). The resulting cell-type maps on the x-y plane at the center of slice on the z-

226 axis (at 5 μ m) were visually similar to the previous study (**Supplementary Fig. 17G**). SSAM cell-
227 type signatures showed high expression of their marker genes (**Supplementary Fig. 18-21**) and
228 a high correlation to the cell-type signatures from both the segmentation-based clusters and
229 scRNA-seq clusters (**Supplementary Fig. 17E, F**). Among them, 7 inhibitory and 4 excitatory
230 neuronal cell types showed very high correlation (>0.8) to the segmentation-based neuronal
231 signatures, and also showed distinctive tissue localization patterns (**Fig. 4D, E**), similar to those
232 previously reported (**Supplementary Fig. 22**).

233
234 We then quantified the similarity of the SSAM cell-type maps with the cell segmentation by
235 Moffitt et al. The SSAM guided mode cell-type map achieved high matching scores for
236 comparable cell types (mean and median of 0.76 and 0.83 for segmentation-based, 0.88 and
237 0.94 for scRNA-seq-based signatures, respectively), with only 6 of 76 cell-types exhibiting a low
238 matching score (< 0.3) for segmentation-based case (**Supplementary Table 4, 5,**
239 **Supplementary Fig. 23, 24**). Comparing the SSAM *de novo* cell-type map also yielded high
240 matching scores (mean and median of 0.83 and 0.93, respectively) (**Supplementary Table 6,**
241 **Supplementary Fig. 25**), further validating the computational approach adopted by SSAM to
242 identify *de novo* cell-type signatures and generating cell-type maps. One of the most notable
243 differences in the SSAM cell-type map was that we found a higher density of astrocytes
244 compared to Moffitt et al. A comparative analysis revealed that some astrocyte signals identified
245 by SSAM were not found in the segmentation by Moffitt et al. Note that the existence of
246 astrocytes is clearly shown by the corresponding marker gene expression (**Supplementary Fig.**
247 **26**).

248
249 The generated tissue domain map identifies several domains consisting of regions consisting
250 primarily of inhibitory neurons, excitatory neurons and oligodendrocytes, as well as the ventricle

251 structure (**Supplementary Fig. 27**).

252

253 Finally, we reconstructed a three-dimensional cell-type map (**Movie 1**). While the thickness of
254 the tissue image is limited (10 μm), we demonstrate the shape and size difference of the whole
255 cell-type map and the cell-type specific maps for inhibitory neurons, excitatory neurons and
256 astrocytes (**Movies 2, 3, 4**).

257

258 Despite the difference of dimensionality between the osmFISH data (2D) and the MERFISH
259 data (3D), SSAM was able to successfully process the data and produce meaningful results.
260 More importantly, the analyzes in this section were performed with almost the same procedure
261 and parameters applied to the osmFISH data. Therefore, we set these parameters as the
262 default values to facilitate rapid and robust analysis of other multidimensional *in situ*
263 transcriptomics dataset using SSAM.

264

265 **SSAM identifies rare cell types and novel cortical sub-layering in the adult mouse visual** 266 **cortex (VISp)**

267 To further demonstrate that SSAM can be used for rapid and robust analysis of *in situ*
268 transcriptomics data, we applied SSAM to unpublished multiplexed smFISH data of the mouse
269 primary visual cortex (VISp) generated as part of the SpaceTx consortium³² (**Fig. 5, 6,**
270 **Supplementary Fig. 28, 29**). In total, the expression of 22 genes was quantified *in situ*
271 (Methods).

272

273 Analysis of the tissue image was restricted to the manually defined VISp region
274 (**Supplementary Fig. 28D**). SSAM was performed in both guided mode and *de novo* mode
275 (**Supplementary Fig. 29A**). The guided mode of SSAM was performed using scRNA-seq data³⁰.
276 For the *de novo* run, the identified cell-type signature clusters were assigned the label of the

277 cluster in the scRNA-seq data with the highest correlation (**Fig. 5A, B**). Then, the tissue
278 domains were identified based on the *de novo* cell-type map (**Fig. 6**), with the result showing the
279 laminar structure of the VISp region. We identified two distinct layer 4 (L4) neuronal clusters.
280 Interestingly, both of them showed the highest correlation to the single L4 IT type identified via
281 scRNA-seq, but their spatial locations show a clear difference (**Fig. 5C, Supplementary Fig.**
282 **29B**). We named the cluster localizing to the superficial region of layer L4 as ‘L4 IT Superficial’
283 (L4 IT 2). This finding adds context to the previously observed heterogeneity of the L4 IT cell
284 type³⁰, where we show that this heterogeneity determines superficial and deep localization in
285 layer 4.

286
287 The cell-type map generated by SSAM guided mode were visually similar to that of *de novo*
288 mode, except for the cell types found in the layer 2 (L2) (**Supplementary Fig. 29A**). We found
289 that the majority of cell types found in L2 were assigned to the VLMC type in SSAM guided
290 mode. We observed that this type was actually a neuronal type in L2. This cell type showed high
291 expression of *Alcam*, a marker gene of the VLMC cell type, but low expression of other genes.
292 Due to the limited number of genes profiled in the multiplexed smFISH experiment, lack of other
293 neuronal marker genes led to incorrect high correlation of this type VLMC. However, SSAM
294 properly assigned the centroid to be L2 neurons in *de novo* mode.

295
296 SSAM was also able to identify a rare cell type, Sst Chodl, which is known to be related to long-
297 range projection and sleep-active neurons³³⁻³⁵. In addition, we mapped the Sst Chodl cell-type
298 signal to between layer L5 and L6 (**Supplementary Fig. 29C**), consistent with previously
299 reported localization to L5 and L6³³. This finding was validated against its marker gene
300 expression (**Supplementary Fig. 30-32**), and ultimately demonstrates SSAMs ability to identify
301 cell-type signatures of lowly abundant and rare cell-types.

302

303 **Discussion**

304 We describe a segmentation-free computational framework for processing *in situ*
305 transcriptomics data and demonstrate its performance on three different adult mouse brain
306 datasets: the somatosensory cortex (SSp) profiled by osmFISH, the hypothalamic preoptic
307 region (POA) by MERFISH, and the visual sensory cortex (VISp) by multiplexed smFISH. We
308 find that the cell-type signatures and maps generated by SSAM for both osmFISH and
309 MERFISH datasets were similar to the previously reported ones, validating the underlying
310 methodology of SSAM. Based on this, we successfully determined cell types and constructed
311 cell-type and tissue domain maps in the multiplexed smFISH mouse VISp dataset.

312
313 In the osmFISH dataset our method outperforms the original segmentation-based cell-type map
314 reconstruction due to limitations in the segmentation process. In the MERFISH dataset we show
315 that SSAM is able to identify diverse populations of cell types and that SSAM is scalable to 3D
316 image data. For the VISp multiplexed smFISH dataset, SSAM identified a rare cell type and
317 elucidated a suspected spatial heterogeneity of cell types in the cortex without segmenting a
318 single cell. Overall, the results show that SSAM is not only a robust tool to validate
319 segmentation-based methods, but also a reasonable alternative when segmentation is difficult
320 or DAPI or Poly-A images are lacking.

321
322 However, for some questions it is important to distinguish between cells to e.g. delineate growth
323 arising from increasing cell size vs cell proliferation or to investigate multinucleation in
324 cardiomyocytes or cytotrophoblast cells. In cases such as these, we recommend the use of
325 SSAM as a complementary method to segmentation-based analysis in two ways. First, the
326 output of SSAM can be compared to validate that the segmentation process did not introduce
327 artifacts. Secondly, to use the SSAM output as an input for the segmentation process to refine
328 the segmentation procedure for different domains or cell-type signals.

329
330 In terms of methodological parsimony, SSAM minimizes the number of assumptions, avoids
331 iterative optimization and thus offers maximal transparency, interpretability and reproducibility.
332 The lightweight nature of the algorithm typically brings a considerable runtime advantage over
333 other available packages. SSAM is written as a Python library, with some core analysis
334 functions wrapped up with external C functions to speed up the computation. The package is
335 available as an easily installable Python package, and can easily be extended with existing *in*
336 *situ* transcriptomics pipelines, e.g. starfish (<https://github.com/spacetx/starfish>) or Giotto³⁶.
337 SSAM is accompanied with a notebook outlining all the steps presented in this paper. Taken
338 together, we present a novel, flexible and robust method for fully automated cell-type and tissue
339 domain analysis that is readily applicable to numerous *in situ* transcriptomics methods.

340

341 **Materials and Methods**

342

343 **Using Kernel Density Estimation to generate the gene expression vector field**

344 We used the n-dimensional KDE algorithm to estimate the density of mRNAs in 2D and 3D. To
345 compute Gaussian KDE, we used our own implementation of the KDE algorithm for rapid
346 computation. Spatial distribution of the probability of mRNA presence \hat{p} is estimated using the
347 kernel density estimation;

348

$$\hat{p}(\mathbf{x}) = \frac{1}{N} \sum_{i=1}^N K_h(\mathbf{x} - \mathbf{x}_i)$$

349

350

351 where:

352 - K_h : a kernel function with a bandwidth h

- 353 - N : the number of data points
- 354 - \mathbf{x}_i : location vector of the data point i (i.e. location of i -th mRNA)

355

356 Here we use the Gaussian kernel:

357

$$\kappa_h(\mathbf{x}) = \frac{1}{(2\pi h^2)^{d/2}} e^{-\frac{1}{2}\|\mathbf{x}\|^2/h^2}$$

358

359

360 where:

- 361 - h : bandwidth of the Gaussian kernel
- 362 - d : dimension of the space where the data points reside (2 for 2D, or 3 for 3D mRNA
- 363 locations)
- 364 - $\|\mathbf{x}\|$: Euclidean norm (i.e. L2 norm) of vector \mathbf{x}

365 Note that the integration of $\hat{p}(\mathbf{x})$ all over the space is 1. Therefore the gene expression density

366 is calculated by multiplying the number of mRNAs per gene to \hat{p} .

367

368 **Calculation of spatial gene expression**

369 The continuous estimation of gene expression density is discretized over pixels of the tissue

370 image, which in our examples is set to a size of $1 \mu\text{m}$. The expectation value of the estimated

371 density in a unit pixel is approximated by multiplying the area of the unit pixel to the estimated

372 gene expression density at the location of the pixel. Finally, we stack the estimated gene

373 expression densities of genes to define the gene expression vector field over the image.

374

375 **Selection of local maxima**

376 Local maxima were selected based on the L1-norm of the vectors in the vector field, which is

377 the total size of each vector in the image. For the selection algorithm, we used scikit-image
378 Python package to select local maxima. Briefly, 1) maximum filter is applied to dilate the original
379 image, 2) the locations where the maximum filtered image equal to the original image are
380 selected. The maximum filter with size 3 was used throughout the examples presented in this
381 paper.

382 383 **Downsampling of the vector field**

384 For a scalable cell-type identification analysis, the vector field is downsampled to a smaller set
385 of vectors based on local maxima selection strategy (Supplementary discussion). SSAM applies
386 two thresholds for local maxima selection: 1) a minimum expression threshold for a single gene
387 defined as the height of a single Gaussian kernel to avoid regions with signal from only the
388 Gaussian tail (see Discussion section for details), which also corresponds to the position of the
389 observable drop in the histograms of gene expression (**Supplementary Fig. 3A, 17A, 28A**); 2)
390 a minimum total gene expression (i.e. L1-norm) threshold (**Supplementary Fig. 3B, 17B, 28B**).
391 Furthermore, we implemented an optional “input mask” feature to limit sampling of vectors to
392 regions of the image containing informative data, e.g. a mask outlining the informative tissue
393 area.

394 395 **Comparison of local maxima and random sampling strategies**

396 The two local maxima sampling methods, 1) local maxima sampling and 2) random
397 downsampling, were compared to justify our preference of local maxima sampling method for
398 the downstream analysis. The osmFISH data was used for the comparison. Firstly 11,469 local
399 maxima vectors were found in the vector field using a window size of 3, a minimal gene
400 expression and L1 norm thresholding. For comparison, the same number of vectors were
401 randomly sampled from the vector field, using the same thresholds used for local maxima
402 selection. At the locations of the vectors, both the local maxima and the random sampled

403 locations, the classified cell types on the cell-type map guided by segmentation-based
404 signatures are called. For each case, the Pearson's correlation coefficients between the vectors
405 and the signature of the cell types are calculated and plotted as a distribution (**Supplementary**
406 **Fig. 39**).

407

408 **Variance stabilization of local maxima vectors and the vector field**

409 Since the gene expression profiles of local maxima vectors are representative of the
410 transcriptomes of cells, we considered them to be analogous to the gene expression count
411 matrix obtained from single cell RNA sequencing (scRNA-seq) using unique molecular
412 identifiers (UMI). Therefore, we normalized the local maxima vectors of the vector field (which
413 would be representative of single cells) using *sctransform*³⁷, a normalization and regularization
414 algorithm for UMI count data. After that, each vector of the vector field is normalized using
415 *sctransform*, with the same parameters previously used to normalize the local maxima.

416

417 **Clustering of representative gene expression vectors**

418 The SSAM framework supports clustering via DBSCAN²⁴, HDBSCAN²⁵, OPTICS²⁶ and an
419 implementation of the Louvain algorithm equivalent to that in the R package, Seurat²⁷. DBSCAN,
420 HDBSCAN and OPTICS are implemented via the scikit-learn Python library. The Louvain
421 clustering algorithm is based on the R package Seurat²⁷ reimplemented in Python. In short, an
422 SNN network with correlation metric is built using a python package NetworkX³⁸. The weight of
423 the network is calculated by a Jaccard similarity coefficient. A weight smaller than 1/15 was set
424 to zero. Clustering was done by detecting communities in the network using a Louvain
425 community detection algorithm implemented in Python (python-louvain, [https://python-](https://python-louvain.readthedocs.io/)
426 [louvain.readthedocs.io/](https://python-louvain.readthedocs.io/)). It is known that the Louvain algorithm is not sensitive in detecting small
427 clusters³⁹, optionally DBSCAN algorithm can be applied to subcluster each Louvain cluster. This
428 sub-clustering strategy is conceptually similar to the "Polished Louvain" algorithm in Zeisel et

429 al³¹.

430

431 **Diagnostic plots**

432 After unsupervised clustering of gene expression vectors, some clusters may need to be
433 manually merged or discarded. SSAM supports merging of clusters based on correlation of
434 gene expression profile, however in many cases manual inspection is needed to rule out any
435 non-trivial issues. To guide this process, SSAM generates a cluster-wise 'diagnostic plot', which
436 consists of four panels: 1) location of the clustered vectors on the tissue image, 2) the pixels
437 classified to belong the cluster signature (the cluster centroid), 3) the mean expression profile of
438 the clustered vectors, and 4) the t-SNE or UMAP embedding.

439

440 In the three datasets analyzed the clusters to be merged or removed often showed a
441 discordance between the location of sampled vectors used to determine the cluster (panel 1)
442 and the pixels classified to belong to that cluster (panel 2). In case of overclustering, i.e. when a
443 cell-type signature is split over 2 clusters, the map typically does not classify the full shape of
444 the cells but instead only fragments (panel 2), and having almost the same marker gene
445 expression of another cluster (panel 3). Such clusters can be merged. For dubious clusters that
446 should be removed, we observed that vectors usually originate from outside the tissue region or
447 from image artifacts (panel 1), or that the gene expression does not show any clear expression
448 of marker genes or similarity to expected gene expression profiles (panel 3).

449 The remaining clusters are then annotated by comparing cluster marker genes to known cell-
450 type markers. Note that in many cases, the identity of clusters can be easily assigned by
451 comparing the centroids of the clusters to the known cell-type signatures, e.g., from single cell
452 RNA sequencing. To support rapid annotation of cell types to clusters, SSAM additionally shows
453 the highest correlating known cell-type signature should this data be available in panel 3. The
454 diagnostic plots for osmFISH, MERFISH, and multiplexed smFISH data are available online in

455 the Jupyter notebook uploaded to zenodo (<http://doi.org/10.5281/zenodo.3478502>).

456

457 **Statistical evaluation of cell-type mapping**

458 The accuracy of the SSAM cell-type map was validated by comparing the published osmFISH
459 segmentation and the SSAM *de novo* cell-type map by two different methods.

460

461 Firstly, to quantitatively compare concordance of cell-type we implemented a matching score.

462 The matching score for any given cell type is defined as the number of segmented cells with at
463 least 10% of matched with the SSAM guided or *de novo* mode cell type map of the
464 corresponding cell type of the segment, divided by the total number of segments of the cell type
465 which represents the ratio of segments identified by SSAM. The threshold of 10% was
466 empirically selected to account for differences in cell location in the tissue, especially for very
467 small cells where subtle changes in cell-type labeling can drastically reduce the overlap within
468 the segmented area.

469

470 Secondly, for evaluation of discrepancies in cell-type locations compared to the original studies,
471 we compare the unique part of each segmentation and SSAM *de novo* cell-type map to the
472 parts that are overlapping in both maps in the osmFISH dataset. The gene expression vectors
473 originating from overlapping parts of the same cell types (**Supplementary Table 3**), were
474 regarded as the ground truth set. Then, two sets of unique vectors were defined: 1) the
475 segmentation-only set, the vectors from the regions occupied by segments excluding the
476 overlap, and 2) the SSAM-only set, the vectors from SSAM cell-type map only regions. The
477 distribution of the gene expression vectors in the overlapping set was then compared to the two
478 unique parts (**Supplementary Fig. 14A**). To compare the accuracy of cell-type mapping of the
479 two unique parts, Pearson's correlation coefficient is calculated between the mean expression

480 of the ground truth set and the vectors in each set (**Supplementary Fig. 14B**).

481

482 **Quantification of doublets**

483 The doublet rates were evaluated by two Python packages, DoubletDetection⁴⁰ and Scrublet⁴¹
484 (**Supplementary Table 8**). As the two algorithms require raw counts as input, the unnormalized
485 raw vectors at local maxima used for clustering analysis were used as input of the two
486 algorithms, as an analogy of the raw counts. For DoubletDetection, the doublet rate was
487 calculated by dividing the number of doublets reported by the number of total local maxima. The
488 doublet rate quantification by both methods was consistent, and negligible in the osmFISH and
489 multiplexed smFISH datasets (average doublet rate of <0.5% for both), and marginal for
490 MERFISH (average doublet rate of 3%).

491

492 **SSAM analysis of osmFISH data**

493 KDE was performed with a bandwidth of 2.5 μm . The individual gene expression threshold and
494 total gene expression threshold for selection of local maxima were 0.027 (the height of a single
495 Gaussian) and 0.04, respectively (**Supplementary Fig. 3A, 3B**). Since the selected local
496 maxima includes many locations outside of the tissue area, we further filtered local maxima
497 based on their local density approximated using the k-nearest neighbor algorithm. More
498 specifically, local maxima with a density lower than 0.002 over the closest 100 local maxima,
499 corresponding to fewer than 100 local maxima in a 126.2 μm radius, were filtered out
500 (**Supplementary Fig. 3C**). The selected local maxima vectors were passed to *sctransform* to
501 determine normalization parameters, after which the whole vector field was normalized.

502

503 In SSAM guided mode, the mRNA count matrix of both the previously segmented cells and the
504 scRNA-seq data were normalized by *sctransform*. The centroid of each of the annotated
505 clusters was used to classify cell types in the vector field, generating a cell-type map guided by

506 prior knowledge.

507

508 In SSAM *de novo* mode, the selected local maxima vectors were clustered using the Louvain
509 algorithm with a resolution of 0.15, resulting in 66 clusters (**Supplementary Fig. 4A**). Distinct
510 clusters representing the same cell types were identified and then manually merged, and
511 spurious clusters were removed, resulting in a total of 30 clusters (**Fig. 2A, 2B**). For each
512 cluster, the vectors with insufficient correlation to its cluster medoid were excluded from the
513 centroid calculation (**Supplementary Fig. 1B**). The cluster centroids were compared to that of
514 the segmentation-based (**Supplementary Fig. 4B**) and scRNA-seq cell-type signatures
515 (**Supplementary Fig. 4C**) using Pearson's correlation coefficient. The *de novo* clusters were
516 named after the highest correlating segmentation-based cluster. Note that clusters closest
517 mapped to Inhibitory IC and Inhibitory CP cell types do not only appear in the internal capsule
518 and caudoputamen, but also in the cortex. Therefore, we renamed these clusters to Inhibitory
519 Kcnip2 (since Kcnip2 was the third most expressed gene for this cluster) and Inhibitory Rest,
520 respectively. After classification of the local maxima, we quantified the doublet rates (Methods,
521 **Supplementary Table 8**).

522

523 Tissue domain analysis was performed using a sliding circular window with radius 100 μm with
524 a step of 10 μm . The cell-type proportions from each window were clustered using
525 agglomerative hierarchical clustering with 15 clusters as an initial estimate, subsequently
526 merging the clusters with correlation coefficients higher than 0.8. Spatially connected clusters
527 with a correlation coefficient higher than 0.6 were merged. The resulting domain map was
528 resized to match the size of the cell-type map, after which the cells in different domains were
529 colored.

530

531 **Quantification of mRNA abundance in astrocytes and other brain cell types for osmFISH**

532 **data interpretation**

533 The “L5_All.loom” loom object containing scRNA-seq expression data of half a million cells from
534 the mouse nervous system³¹ was downloaded (<http://mousebrain.org/downloads.html>). The total
535 number of mRNA molecules per cell were extracted and aggregated by their level 2 class labels
536 (astrocytes, immune, vascular, ependymal, neuronal, peripheral glia and oligodendrocyte cells)
537 using Python. The counts were log normalized and subsequently followed a normal distribution
538 (tested using the Shapiro-Wilk test for normality, all *p-values* < 1 x 10e-4 for each class),
539 therefore a Student’s t-test was applicable. For each of the two classes of interest
540 (‘Astrocytes’, ‘Immune’), we performed independent log-space t-tests for unequal sample sizes
541 and unequal variance against each of the other classes. Both astrocyte and immune cell
542 classes have significantly lower mRNA molecule counts compared to other cell types (all *p-*
543 *values* < 1 x 10e-12). While the distribution of mRNA counts in log space followed a normal
544 distribution, the use of a Student’s t-test for large numbers may be not appropriate. Hence, we
545 also describe the difference in their distributions. For both astrocyte and immune cell classes,
546 more than half of the cells of each class exhibited a lower UMI count than the lowest quartile of
547 any other cell class.

548

549 **SSAM analysis of MERFISH data**

550 KDE was performed with bandwidth 2.5 μ m. Local maxima were filtered using a gene
551 expression threshold of 0.0055, and then filtered with total gene expression threshold of 0.0035
552 (**Supplementary Fig. 17A, B**). The selected local maxima vectors were passed to *sctransform*
553 to determine normalization parameters, after which the whole vector field was normalized.

554

555 In SSAM guided mode, the mRNA count matrix of both the previously segmented cells and the
556 scRNA-seq data were normalized by *sctransform*. The centroid of each of the annotated

557 clusters was used to classify cell types in the vector field, generating a cell-type map guided by
558 prior knowledge.

559

560 For SSAM *de novo* mode, the selected vectors were clustered using the Louvain algorithm with
561 a resolution of 0.15, resulting in 68 clusters (**Supplementary Fig. 17C**). By manual inspection of
562 gene expression and localization, overclustering was merged, and spurious clusters were
563 removed, resulting in a total of 50 clusters (**Fig. 2A, 2B**). For each cluster, the vectors that did
564 not have high correlation to its cluster medoid were excluded from the centroid calculation
565 (**Supplementary Fig. 1B**). The centroids of the clusters are compared with that of the
566 segmentation-based clustering result and scRNA-seq result using Pearson's correlation
567 coefficient (**Supplementary Fig. 17E, F**). The SSAM *de novo* clusters correlating best to
568 inhibitory and excitatory neurons were named based on the most highly expressed gene of each
569 cluster, and the non-neuronal clusters were named based on the previous study⁵. After
570 classification of the local maxima, we quantified the doublet rates (Methods, **Supplementary**
571 **Table 8**). We noticed a number of small blobs on the cell type map, which are resultant from
572 cells on a different plane in the 3D image (**Movie 2**). After classification of the local maxima, we
573 quantified the doublet rates (Methods, **Supplementary Table 8**).

574

575 Tissue domain analysis based on the cell-type map was performed using a sliding spherical
576 window with radius 100 μm with a step of 10 μm . The cell-type proportions from each window
577 were clustered using agglomerative hierarchical clustering with 20 clusters as an initial estimate,
578 subsequently merging the clusters with correlation coefficient higher than 0.8. The resulting
579 domain map was resized to match the size of the cell-type map, after which the cells in different
580 domains were colored.

581

582 **Comparison of localization of inhibitory and excitatory neurons**

583 For a number of inhibitory and excitatory neuronal subtypes identified in the posterior POA
584 tissue image using SSAM *de novo* mode, we identified the best matching cell types based on
585 Pearson correlation of their gene expression signatures (**Supplementary Fig. 17F**). We
586 matched the following cell types: SSAM cluster 39 (C39) called Inhibitory Coch to Moffitt cluster
587 I-12, C16 Inhibitory Arhgap36 to I-13, C45 Inhibitory Isr4 to I-15, C34 Inhibitory Calcr to I-14 ,
588 C14 Inhibitory Gda to I-23, C19 Excitatory Cbln1-Cbln2 to E-19, C42 Excitatory Omp to E-16,
589 C25 Excitatory Necab1-Gda to E-9, C8 Excitatory Necab1 to E-14, and C36 Excitatory Col25a1
590 to E-24. For these cell types we checked the tissue localizations reported in the previous studies
591 figures 5a, 5c, 5e, 6b, 6d, and S17⁵. Side-by-side comparison of the localization of these
592 neuronal cell types revealed very similar patterns of localization computed by SSAM and the
593 original publication (**Supplementary Fig. 22**).

594

595 **3D modelling of MERFISH cell-type maps**

596 Firstly, the connected components in 3D were determined using the python package connected-
597 components-3d (<https://github.com/seung-lab/connected-components-3d>). Components
598 comprising fewer than 100 voxels were removed. After this, the voxels filling connected
599 components were removed, and only the contours were used for the vertex of the 3D models.
600 For each vertex, the vertex normal was calculated by simple physics simulation, assuming that
601 the direction of a vertex normal vector is the same as the force vector when there are pulling
602 forces between all of the contour voxels. The surface of the objects was reconstructed using
603 screened Poisson reconstruction algorithm^{42,43} using default parameters. The number of
604 vertices was reduced to 5% of the total number of vertices using the 'vtkQuadricDecimation'
605 function^{44,45} of VTK library⁴⁶. Finally, the objects were merged into a single file. Each scene of
606 the rotating movie was created using Meshlab⁴⁷.

607

608 **VISP multiplexed smFISH data generation**

609 Multiplexed smFISH data of the mouse primary visual cortex (VISp) was generated as part of
610 the SpaceTx consortium. Tissue processing was carried out as previously described⁴⁸, with
611 some modifications.

612

613 Silanization of coverslips (#1.5, Thorlabs CG15KH) was performed by plasma cleaning for 30
614 min in a Plasma-Prep III (SPI 11050-AB), followed by vapor deposition of 3-
615 aminopropyltriethoxysilane (APES, Sigma A3648) in a vacuum for 10 minutes. Coverslips were
616 then washed in 100% methanol for 2 x 5 minutes, allowed to dry, and stored in a dust-free
617 environment until use.

618

619 Fresh-frozen mouse brain tissue was sectioned at 10 μ m onto silanized coverslips, let dry for 20
620 min at -20°C, then fixed for 15 min at 4 °C in 4% PFA in PBS. Sections were washed 3 x 10 min
621 in PBS, then permeabilized and dehydrated with chilled 100% methanol at -20°C for 10 min and
622 allowed to dry. Sections were stored at -80 °C until use. Frozen sections were rehydrated in 2X
623 SSC (Sigma 20XSSC, 15557036) for 5 min, then treated 10 min with 8% SDS (Sigma 724255)
624 in PBS at room temperature. Sections were washed 5 times in 2X SSC. Sections were then
625 incubated in hybridization buffer (10% Formamide (v/v, Sigma 4650), 10% dextran sulfate (w/v,
626 Sigma D8906), 200 μ g/mL BSA (ThermoFisher AM2616), 2 mM ribonucleoside vanadyl
627 complex (New England Biolabs S1402S), 1 mg/ml tRNA (Sigma 10109541001) in 2X SSC) for 5
628 min at 37°C. Probes were diluted in hybridization buffer at a concentration of 250 nM and
629 hybridized at 37°C for 2 h. Following hybridization, sections were washed 2 x 10 min at 37°C in
630 wash buffer (2X SSC, 20% Formamide), and 1 x 10 min in wash buffer with 5 μ g/ml DAPI
631 (Sigma 32670), then washed 3 times with 2X SSC. Sections were then imaged in Imaging buffer
632 (20 mM Tris-HCl pH 8, 50 mM NaCl, 0.8% glucose (Sigma G8270), 30 U/ml pyranose oxidase
633 (Sigma P4234), 50 μ g/ml catalase (Abcam ab219092). Following imaging, sections were

634 incubated 3×10 min in stripping buffer (65% formamide, 2X SSC) at 30°C to remove
635 hybridization probes from the first round. Sections were then washed in 2X SSC for 3×5 min at
636 room temperature before repeating the hybridization procedure.

637
638 The multiplexed smFISH image data was collected and processed using methods previously
639 described⁴⁸, except that images from different rounds of hybridization were registered in (x, y)
640 based on the DAPI signal. The raw images are available on request.

641

642 **SSAM analysis of VISp multiplexed smFISH data**

643 KDE was performed with bandwidth 2.5 μ m. Local maxima were filtered using a gene
644 expression threshold of 0.027, and then filtered with total gene expression threshold of 0.2
645 (**Supplementary Fig. 28A, B**). The selected local maxima vectors were passed to *sctransform*
646 to determine normalization parameters, after which the whole vector field was normalized. To
647 identify rare cell types expected to exist in this tissue, the initial clustering result by Louvain
648 algorithm was sub-clustered by DBSCAN (Method). Initially 49 clusters were obtained with a
649 resolution parameter of 0.15. By manual inspection, several over-clustered cell types, including
650 nine L2/3 IT 1, two L2/3 IT 2, six L4 IT 2, six L6 CT, and two L6 IT 2 clusters were merged, and
651 one spurious cluster was removed, resulting in 28 clusters. The centroids of the clusters are
652 compared with that of scRNA-seq result using Pearson's correlation coefficient
653 (**Supplementary Fig. 28E**). The clusters were named after the highest correlating scRNA-seq
654 cluster, except the newly found 'L4 IT Superficial' (L4 IT 2) cluster. After classification of the
655 local maxima, we quantified the doublet rates (Methods, **Supplementary Table 8**).

656

657 Tissue domains were defined using a sliding circular window with radius 100 μ m with step of 10
658 μ m over the cell-type map image. Cell type compositions of the windows were clustered using
659 agglomerative clustering, initially with 20 clusters. Clusters with Pearson's correlation higher

660 than 0.7 were merged to result in nine clusters. Further, two clusters were merged since they
661 were different parts of the Pia layer, resulting in a final set of seven clusters representing tissue
662 domains (**Fig. 6**).

663

664 **Plotting**

665 The python packages Matplotlib 3.1.0⁴⁹ and Seaborn 0.9.0⁵⁰ were used to draw 2D images,
666 plots, and heatmaps. We include helper functions in SSAM to easily generate plots.

667

668 **Movies**

669 Movies were generated by using Virtualdub (1.10.4-AMD64, <http://www.virtualdub.org/>). The
670 H.264 codec was used to compress videos.

671

672 **Software**

673 Python version 3.7.0 was used throughout. The following python packages were used:
674 *numpy*, *scipy*, *pandas*, *matplotlib*, *seaborn*, *scikit-learn*, *umap-learn*, *python-louvain*, *sparse*,
675 *scikit-image*. R package *sctransform* was used for normalization and variance stabilization of
676 the data.

677

678 **Data availability**

679 The source code of SSAM is available online at <https://github.com/eislabs/ssam>. A Jupyter
680 notebook (https://github.com/eislabs/ssam_example) outlines the commands used to download
681 and pre-process the data, and to reproduce the results and figures of this study. The Jupyter
682 notebooks also contain the extensive diagnostic plots used for parameter selection, and choice
683 of removal or merging of clusters. All large files are available online from
684 <http://doi.org/10.5281/zenodo.3478502>.

685

686 The osmFISH data (Codeluppi et al., 2018) used within the study is available from
687 <http://linnarssonlab.org/osmFISH/availability/>. The single cell RNA sequencing data of the
688 mouse somatosensory cortex^{28,29} are available from <http://loom.linnarssonlab.org/>. The single
689 cell RNA sequencing data³¹ used to compare total mRNA molecules between cell types are
690 available from <http://mousebrain.org/>. The high resolution poly-A and DAPI images of osmFISH
691 data (Codeluppi et al., 2018) were kindly provided by Sten Linnarsson. The MERFISH data
692 (Moffitt et al., 2018) is available from <https://datadryad.org/handle/10255/dryad.192644>. Mouse
693 VISp multiplexed smFISH data are available from <http://doi.org/10.5281/zenodo.3478502>.
694

695 **Acknowledgements**

696 We thank Sten Linnarsson and Jeffrey Moffitt for providing support and access to the osmFISH
697 and MERFISH datasets, respectively. We also thank Yue Zhuo, Ed Lein, Jeremy Miller,
698 Ambrose Carr, Nagarajan Paramasivam, Stephen Krämer, Zuguang Gu, Daniel Hübschmann,
699 Luca Tosti, and Christian Conrad for helpful discussions and comments on data analysis. The
700 authors also thank Bianca Hennig for designing Figure 1, and assistance in improving figures.
701 The preliminary analysis of multiplexed smFISH data occurred during the SpaceTx SpaceJam
702 Hackathon at the Allen Institute for Brain Science, which was organized by Ed Lein, and
703 generously supported by the Chan Zuckerberg Initiative. This publication is part of the Human
704 Cell Atlas - www.humancellatlas.org/publications. This research has received funding from the
705 European Union's Horizon 2020 research and innovation program under grant agreement No
706 824110 – EASI-Genomics, and was supported by the European Commission (ESPACE,
707 874710, Horizon 2020).

708

709 **Author contributions**

710 JP, WC designed the concept and idea of SSAM.

711 JP, WC, RE, NI conceived the study.

712 BT, EG, TN.N, BL acquired and interpreted the multiplexed smFISH data.

713 JP, WC, ST, TN.N, NI performed data analysis.

714 LE.B, MS, BL, BT, TG, OS provided critical comments and discussions.

715 RE, NI supervised the study.

716 All authors commented on and critically revised the manuscript.

717

718 **Competing interests**

719 The authors declare no competing interests.

720 References

- 721 1. Svensson, V., Vento-Tormo, R. & Teichmann, S. A. Exponential scaling of single-cell RNA-
722 seq in the past decade. *Nat. Protoc.* **13**, 599–604 (2018).
- 723 2. Regev, A. *et al.* Science Forum: The Human Cell Atlas. *Elife* **6**, (2017).
- 724 3. Luecken, M. D. & Theis, F. J. Current best practices in single-cell RNA-seq analysis: a
725 tutorial. *Mol. Syst. Biol.* **15**, e8746 (2019).
- 726 4. Salmén, F. *et al.* Multidimensional transcriptomics provides detailed information about
727 immune cell distribution and identity in HER2+ breast tumors. *bioRxiv* 358937 (2018)
728 doi:10.1101/358937.
- 729 5. Moffitt, J. R. *et al.* Molecular, spatial, and functional single-cell profiling of the hypothalamic
730 preoptic region. *Science* **362**, (2018).
- 731 6. Codeluppi, S., Borm, L. E., Zeisel, A. & La Manno, G. Spatial organization of the
732 somatosensory cortex revealed by osmFISH. *Nature Methods* **15**, 932–935 (2018).
- 733 7. Chen, K. H., Boettiger, A. N., Moffitt, J. R., Wang, S. & Zhuang, X. Spatially resolved, highly
734 multiplexed RNA profiling in single cells. *Science* **348**, aaa6090 (2015).
- 735 8. Lubeck, E., Coskun, A. F., Zhiyentayev, T., Ahmad, M. & Cai, L. Single-cell in situ RNA
736 profiling by sequential hybridization. *Nature methods* vol. 11 360–361 (2014).
- 737 9. Ke, R. *et al.* In situ sequencing for RNA analysis in preserved tissue and cells. *Nat.*
738 *Methods* **10**, 857–860 (2013).
- 739 10. Lee, J. H. *et al.* Fluorescent in situ sequencing (FISSEQ) of RNA for gene expression
740 profiling in intact cells and tissues. *Nat. Protoc.* **10**, 442–458 (2015).
- 741 11. Wang, X. *et al.* Three-dimensional intact-tissue sequencing of single-cell transcriptional
742 states. *Science* **361**, (2018).
- 743 12. Ståhl, P. L. *et al.* Visualization and analysis of gene expression in tissue sections by spatial
744 transcriptomics. *Science* **353**, 78–82 (2016).

- 745 13. Maniatis, S. *et al.* Spatiotemporal dynamics of molecular pathology in amyotrophic lateral
746 sclerosis. *Science* **364**, 89–93 (2019).
- 747 14. Vickovic, S. *et al.* High-definition spatial transcriptomics for in situ tissue profiling. *Nat.*
748 *Methods* **16**, 987–990 (2019).
- 749 15. Hodneland, E., Kögel, T., Frei, D. M., Gerdes, H.-H. & Lundervold, A. CellSegm - a
750 MATLAB toolbox for high-throughput 3D cell segmentation. *Source Code Biol. Med.* **8**, 16
751 (2013).
- 752 16. Salvi, M. *et al.* Automated Segmentation of Fluorescence Microscopy Images for 3D Cell
753 Detection in human-derived Cardiospheres. *Sci. Rep.* **9**, 6644 (2019).
- 754 17. Kong, J. *et al.* Automated cell segmentation with 3D fluorescence microscopy images. in
755 *2015 IEEE 12th International Symposium on Biomedical Imaging (ISBI)* 1212–1215 (2015).
- 756 18. Jiang, J., Kao, P.-Y., Belteton, S. A., Szymanski, D. B. & Manjunath, B. S. Accurate 3D Cell
757 Segmentation using Deep Feature and CRF Refinement. *arXiv [cs.CV]* (2019).
- 758 19. Shah, S., Lubeck, E., Zhou, W. & Cai, L. In Situ Transcription Profiling of Single Cells
759 Reveals Spatial Organization of Cells in the Mouse Hippocampus. *Neuron* **92**, 342–357
760 (2016).
- 761 20. Kishi, J. Y. *et al.* SABER amplifies FISH: enhanced multiplexed imaging of RNA and DNA
762 in cells and tissues. *Nat. Methods* **16**, 533–544 (2019).
- 763 21. Halpern, K. B. *et al.* Single-cell spatial reconstruction reveals global division of labour in the
764 mammalian liver. *Nature* **542**, 352–356 (2017).
- 765 22. Lignell, A., Kerosuo, L., Streichan, S. J., Cai, L. & Bronner, M. E. Identification of a neural
766 crest stem cell niche by Spatial Genomic Analysis. *Nat. Commun.* **8**, 1830 (2017).
- 767 23. Thomas, R. M. & John, J. A review on cell detection and segmentation in microscopic
768 images. 1–5 (2017).
- 769 24. Ester, M., Kriegel, H.-P., Sander, J. & Xu, X. A density-based algorithm for discovering
770 clusters in large spatial databases with noise. in *Proceedings of the Second International*

- 771 *Conference on Knowledge Discovery and Data Mining* 226–231 (AAAI Press, 1996).
- 772 25. McInnes, L., Healy, J. & Astels, S. hdbscan: Hierarchical density based clustering. *JOSS* **2**,
773 205 (2017).
- 774 26. Ankerst, M., Breunig, M. M., Kriegel, H.-P. & Sander, J. OPTICS: ordering points to identify
775 the clustering structure. *SIGMOD Rec.* **28**, 49–60 (1999).
- 776 27. Butler, A., Hoffman, P., Smibert, P., Papalexi, E. & Satija, R. Integrating single-cell
777 transcriptomic data across different conditions, technologies, and species. *Nat. Biotechnol.*
778 **36**, 411–420 (2018).
- 779 28. Zeisel, A. *et al.* Cell types in the mouse cortex and hippocampus revealed by single-cell
780 RNA-seq. *Science* **347**, 1138–1142 (2015).
- 781 29. Marques, S. *et al.* Oligodendrocyte heterogeneity in the mouse juvenile and adult central
782 nervous system. *Science* **352**, 1326–1329 (2016).
- 783 30. Tasic, B. *et al.* Shared and distinct transcriptomic cell types across neocortical areas.
784 *Nature* **563**, 72–78 (2018).
- 785 31. Zeisel, A. *et al.* Molecular Architecture of the Mouse Nervous System. *Cell* **174**, 999–
786 1014.e22 (2018).
- 787 32. Perkel, J. M. Starfish enterprise: finding RNA patterns in single cells. *Nature* **572**, 549–551
788 (2019).
- 789 33. Tasic, B. *et al.* Adult mouse cortical cell taxonomy revealed by single cell transcriptomics.
790 *Nat. Neurosci.* **19**, 335–346 (2016).
- 791 34. Tomioka, R. *et al.* Demonstration of long-range GABAergic connections distributed
792 throughout the mouse neocortex. *Eur. J. Neurosci.* **21**, 1587–1600 (2005).
- 793 35. Gerashchenko, D. *et al.* Identification of a population of sleep-active cerebral cortex
794 neurons. *Proc. Natl. Acad. Sci. U. S. A.* **105**, 10227–10232 (2008).
- 795 36. Dries, R. *et al.* Giotto, a pipeline for integrative analysis and visualization of single-cell
796 spatial transcriptomic data. *bioRxiv* 701680 (2019) doi:10.1101/701680.

- 797 37. Hafemeister, C. & Satija, R. Normalization and variance stabilization of single-cell RNA-seq
798 data using regularized negative binomial regression. *bioRxiv* 576827 (2019)
799 doi:10.1101/576827.
- 800 38. Hagberg, A., Swart, P. & S Chult, D. Exploring network structure, dynamics, and function
801 using NetworkX. in *Proceedings of the 7th Python in Science Conference (SciPy2008)* 11–
802 15 (Los Alamos National Lab.(LANL), Los Alamos, NM (United States), 2008).
- 803 39. Fortunato, S. & Barthélemy, M. Resolution limit in community detection. *Proc. Natl. Acad.*
804 *Sci. U. S. A.* **104**, 36–41 (2007).
- 805 40. Gayoso, A., Shor, J., Carr, A. J., Sharma, R. & Pe'er, D. *JonathanShor/DoubletDetection:*
806 *HOTFIX: Correct setup.py installation.* (2019). doi:10.5281/zenodo.3376859.
- 807 41. Wolock, S. L., Lopez, R. & Klein, A. M. Scrublet: Computational Identification of Cell
808 Doublets in Single-Cell Transcriptomic Data. *Cell Syst* **8**, 281–291.e9 (2019).
- 809 42. Kazhdan, M., Bolitho, M. & Hoppe, H. Poisson surface reconstruction. in *Proceedings of the*
810 *fourth Eurographics symposium on Geometry processing* 61–70 (2006).
- 811 43. Kazhdan, M. & Hoppe, H. Screened poisson surface reconstruction. *ACM Trans. Graph.* **32**,
812 29 (2013).
- 813 44. Garland, M. & Heckbert, P. S. Surface simplification using quadric error metrics. in
814 *Proceedings of the 24th annual conference on Computer graphics and interactive*
815 *techniques* 209–216 (ACM Press/Addison-Wesley Publishing Co., 1997).
- 816 45. Hoppe, H. New quadric metric for simplifying meshes with appearance attributes. in
817 *Proceedings Visualization '99 (Cat. No.99CB37067)* 59–510 (1999).
- 818 46. Schroeder, W., Martin, K. & Lorensen, B. *The Visualization Toolkit: An Object-oriented*
819 *Approach to 3D Graphics.* (Kitware, 2006).
- 820 47. Cignoni, P. *et al.* Meshlab: an open-source mesh processing tool. in *Eurographics Italian*
821 *chapter conference* vol. 2008 129–136 (2008).
- 822 48. Hodge, R. D. *et al.* Conserved cell types with divergent features in human versus mouse

- 823 cortex. *Nature* **573**, 61–68 (2019).
- 824 49. Caswell, T. A. *et al.* *matplotlib/matplotlib v3.1.0*. (Zenodo, 2019).
- 825 doi:10.5281/zenodo.2893252.
- 826 50. Waskom, M. *et al.* *mwaskom/seaborn: v0.9.0 (July 2018)*. (Zenodo, 2018).
- 827 doi:10.5281/zenodo.1313201.
- 828

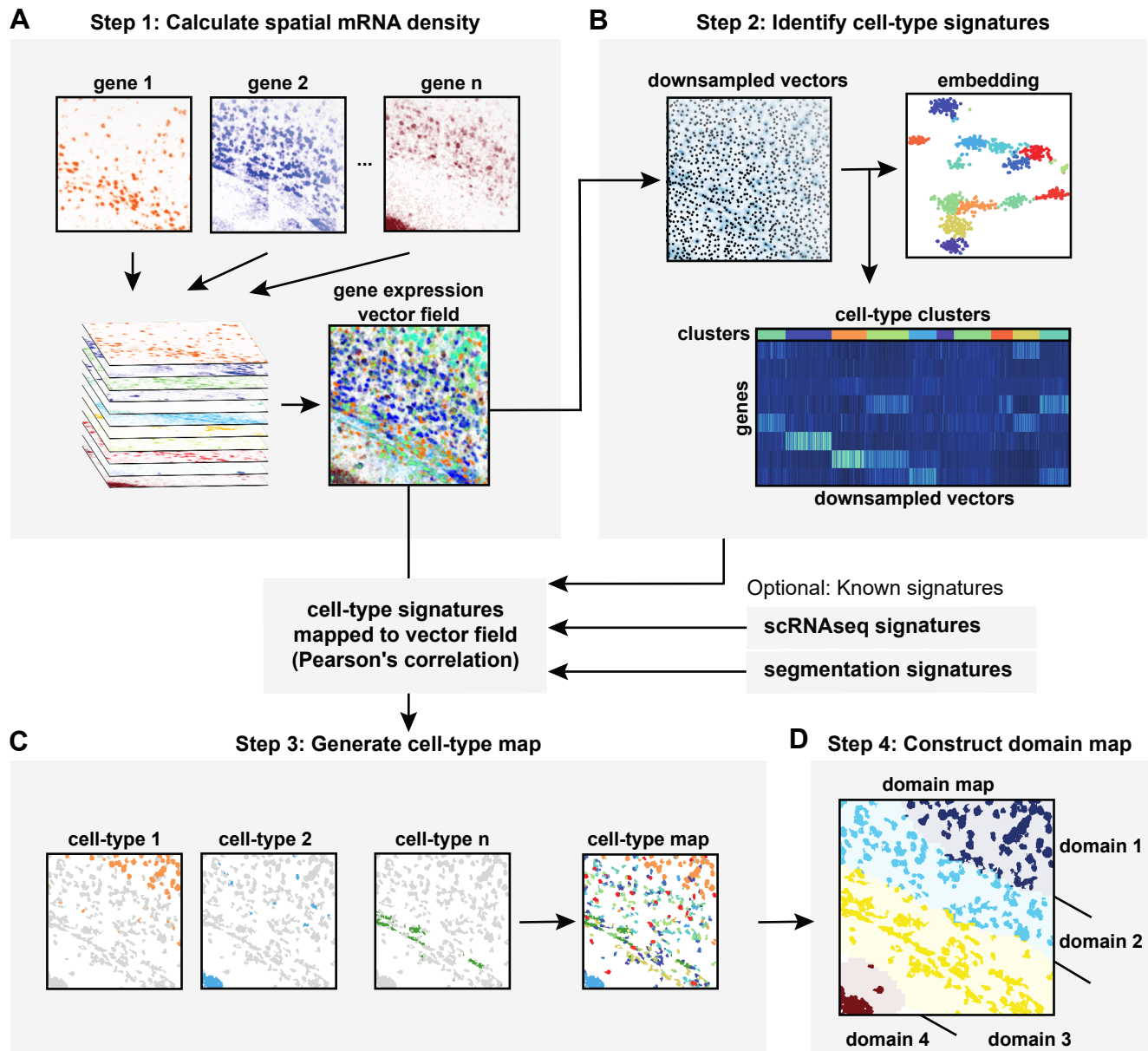


Figure 1. Schematic diagram of the SSAM computational workflow for cell type and tissue domain definition based on gene expression data.

(A) In step 1, SSAM converts mRNA locations into a vector field of gene expression values. For this, SSAM applies a Gaussian KDE to mRNA locations for each gene and projects the resulting mRNA density values to a square lattice which represents coordinates in the tissue. The mRNA density estimated per each gene are stacked to produce a “gene expression vector field” over the lattice. The gene expression vector field is analogous to a 2D/3D image where each pixel/voxel encodes the averaged gene expression of the unit area. Further details of the application of KDE can be found in Supplementary Fig. 1A; (B) In step 2, cell-type signatures are identified *de novo*. First, the gene expression profile at probable cell locations are identified as the local regions in the gene expression vector field where the signal is highest. These downsampled gene expression signals are identified and used for *de novo* cell type identification by cluster analysis. Alternatively, previously defined cell-type signatures can be used. (C) In step 3, a cell-type map is generated. For this, the cell-type signatures are mapped onto the gene expression vector field and cell types are assigned based on Pearson’s correlation between each cell-type expression signature to the vector field to define cell-type distribution *in situ*. Further details about creating the cell-type map can be found in Supplementary Fig. 2A; (D) In step 4, the tissue domains are identified. The tissue domain signatures are identified using a sliding window to compute domain signatures based on the count of cell-type labels in the window. The tissue domains are defined by clustering these signatures. Further details on creating the tissue domain map can be found in Supplementary Fig. 2B.

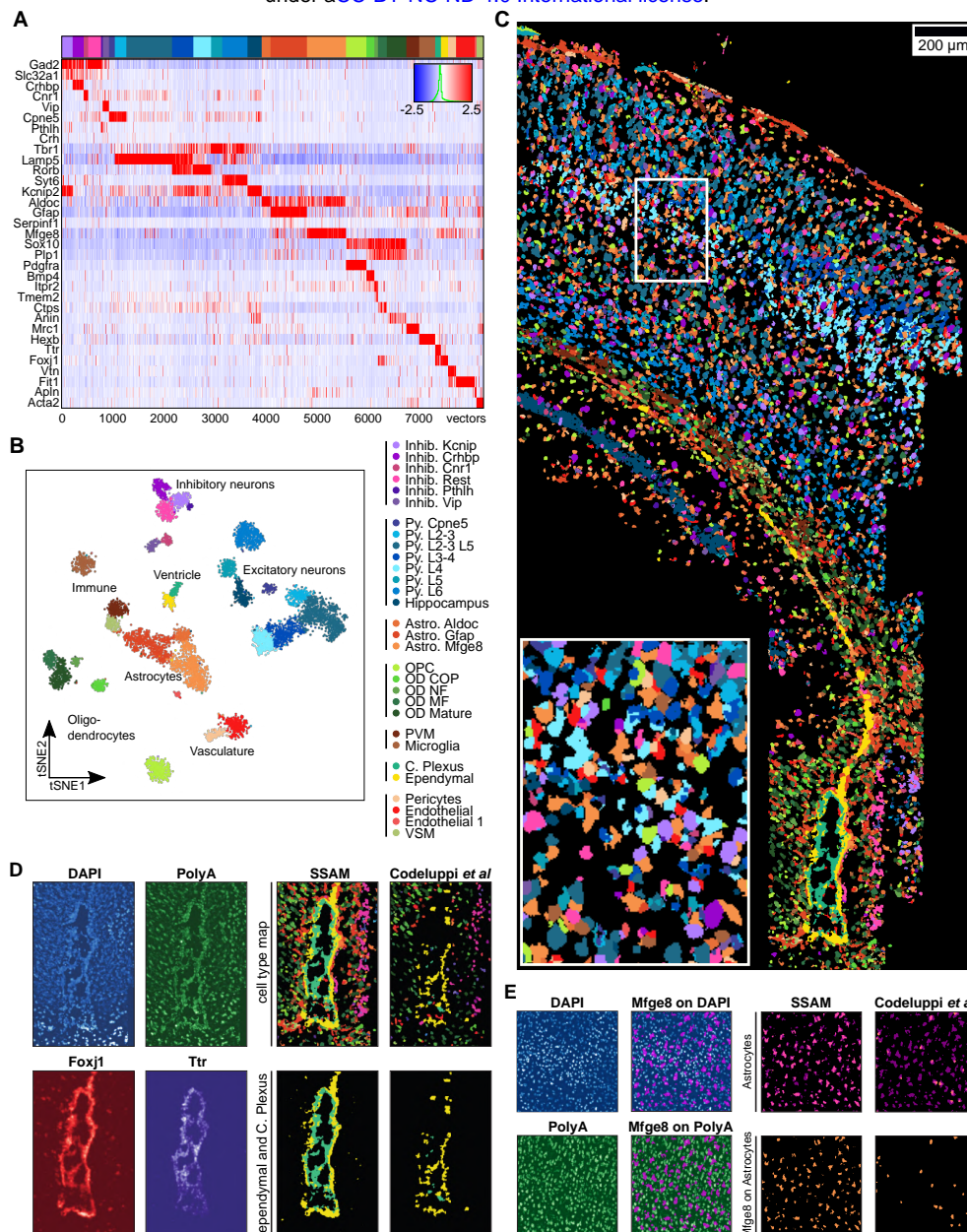


Figure 2. SSAM improves astrocyte and ventricle detection in the mouse SSp region.

(A) Gene expression heatmap showing cell-type specific expression of marker genes (8,252 vectors). Rows show z-score normalized gene expression and columns show the gene expression patterns of filtered local maxima vectors. The top annotation shows the cell types and coloring based on the best correlating segmentation-based cell-type signature from Codeluppi *et al.* The colors of the top annotation correspond to the cell type legend in Fig. 2B; (B) A t-SNE map of cell-type signatures with distinct expression. Cell-type clusters are visualized as a 2D t-SNE embedding of filtered local maxima vectors. Cell-type annotation and coloring are based on the best correlating segmentation-based cell-type signature from Codeluppi *et al.* (Supplementary Fig. 4C,D). The cell-type legend is grouped by cell-type classes labels shown in the tSNE plot, and are based on groupings by Codeluppi *et al.*; (C) The SSAM *de novo* cell-type map showing spatial organization of the cell types signatures in the gene expression vector field. Inset shows a zoom in of the highlighted tissue region. The colors of the cell types correspond to the cell-type legend in Fig. 2B; (D) SSAM improves the reconstruction of the ventricle. The upper left 2 panels show the DAPI and Poly-A signal around the ventricle area, showing tightly packed cells (occlusion) and lower signal in the ventricle structure compared to surrounding cells. The lower left 2 panels show the KDE gene expression signature for *Foxj1* (the marker for ependymal cells) and *Ttr* (the marker for choroid plexus cells). The upper right 2 panels show the cell-type maps reconstructed by SSAM, showing a more complete reconstruction, and by Codeluppi *et al.*, which misses parts of the ventricle structure. The bottom right 2 panels show the reconstructions of only the ependymal (yellow) and choroid plexus (teal) cell types by SSAM and Codeluppi *et al.*; (E) SSAM has increased sensitivity of astrocyte detection. The far left upper and lower panels show DAPI and Poly-A signal for a region in the tissue. The middle left upper and lower panels show the overlap of *Mfge8* signal (a marker for one astrocyte) with DAPI and Poly-A signals, showing that *Mfge8* signal corresponds with low Poly-A signal, but with higher DAPI signal. The top right 2 panels show the cell-type signals for *Mfge8* expressing astrocytes by SSAM and Codeluppi *et al.*, showing that SSAM detect much more astrocyte cell types. The bottom right 2 panels shows the overlay of *Mfge8* signal with the cell-type calls by SSAM and Codeluppi *et al.*, showing the astrocyte signals detected by SSAM correspond well with *Mfge8* signal.

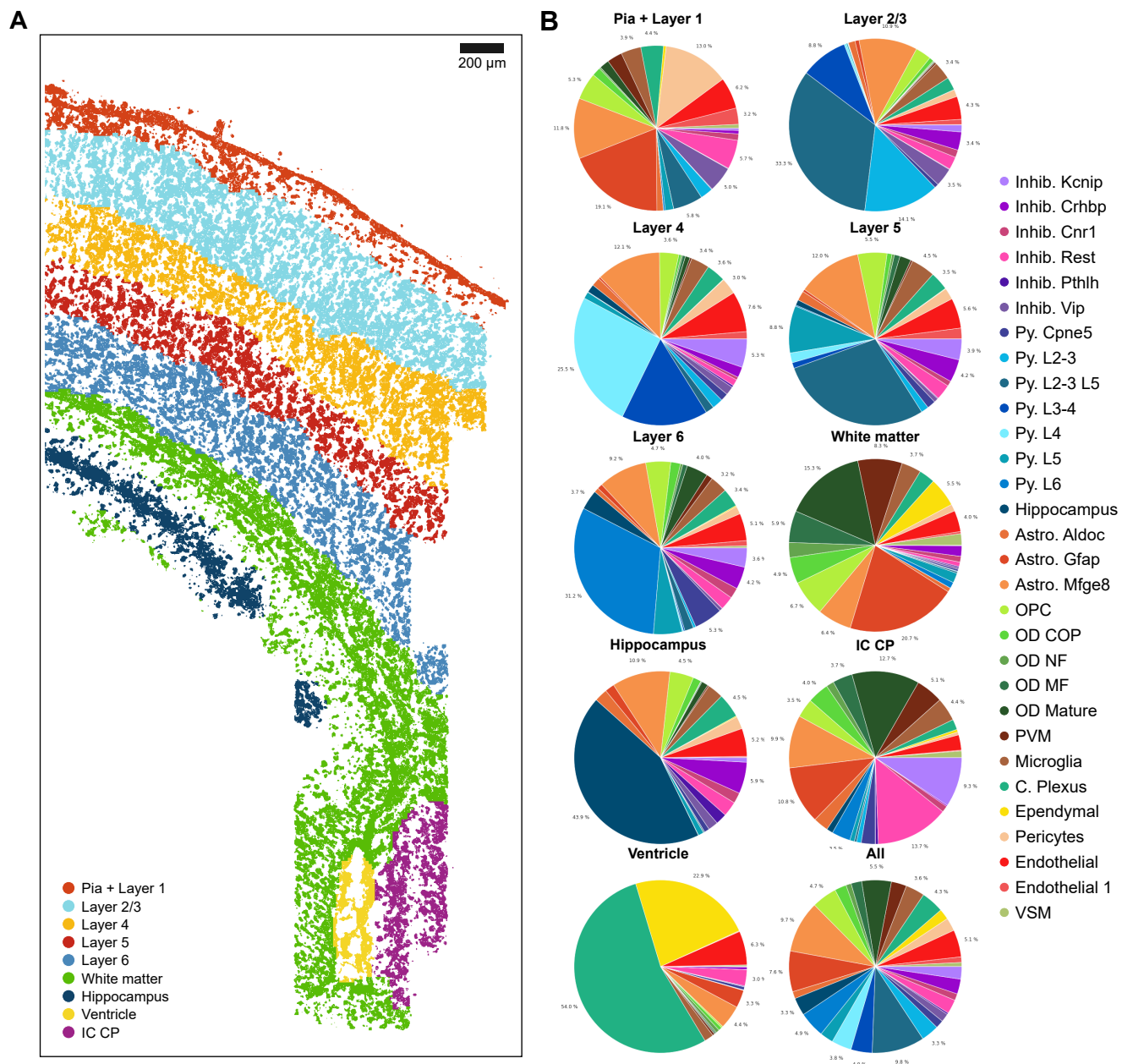


Figure 3. SSAM identifies cortical layer tissue domains in the mouse SSap cortex.

(A) Tissue domain map generated by SSAM. Tissue domain signatures were identified from clustering local cell-type composition over sliding 100 μm circular windows, and projected back onto the cell-type map. The reconstruction shows the various cortical layers; (B) Cell-type composition within each tissue domain. The plots show that each domain consists of 7-14% Astrocyte Mfge8 cell types, apart from the ventricle, which instead shows a majority of Choroid plexus and Ependymal cell types.

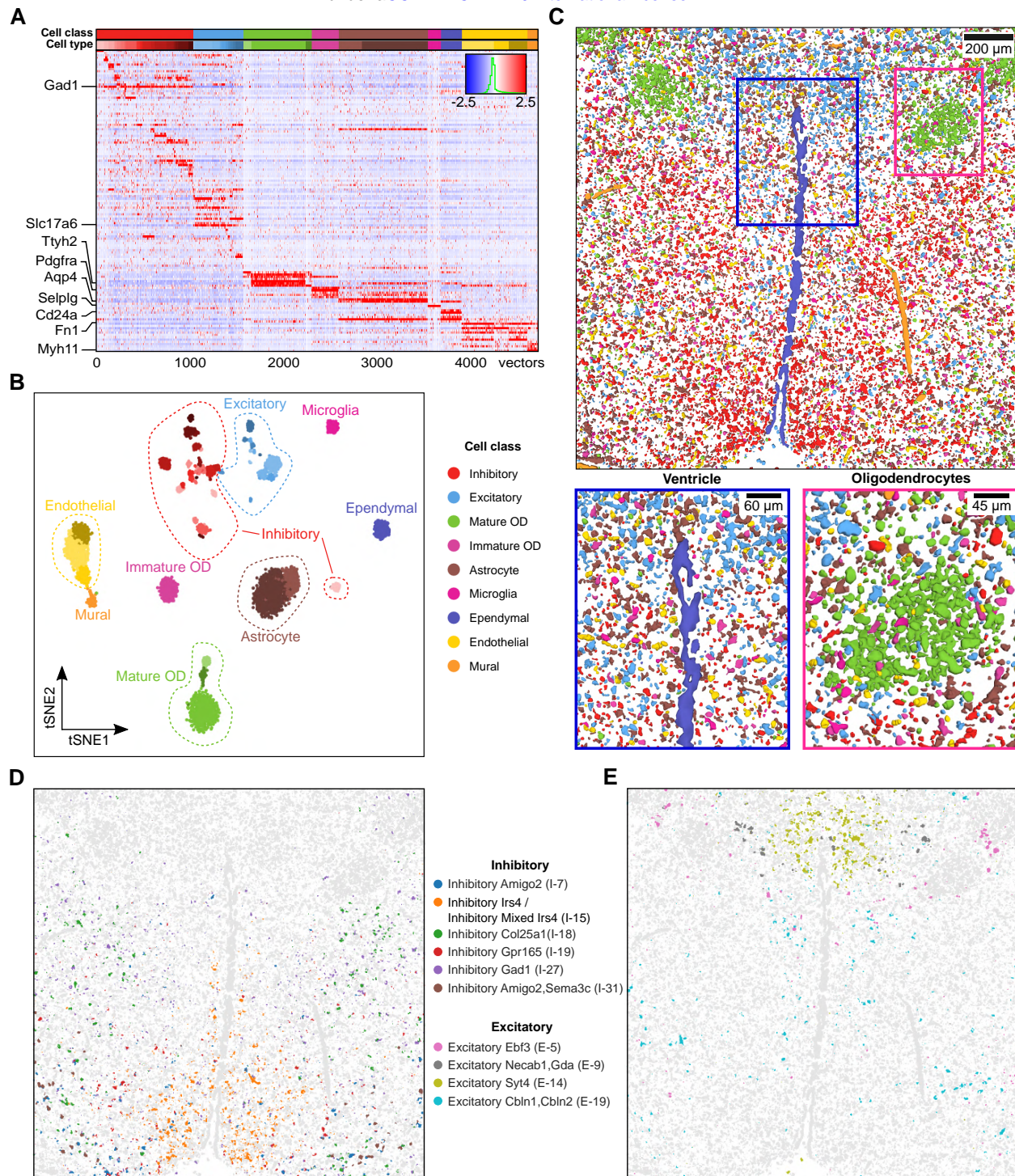


Figure 4. SSAM 3D cell type map confirms rich diversity of heterogeneous cells in the posterior hypothalamic POA.

(A) Gene expression heatmap showing cell-type specific expression of marker genes (4,714 vectors). Rows show z-score normalized gene expression and columns show the gene expression patterns of filtered local maxima vectors (representative of gene expression within a cell). The bottom row of the top annotation shows the cell types. Due to a rich diversity of various inhibitory and excitatory neurons captured, the cell types were grouped into classes. The top row of the top annotation shows the cell classes which are named and colored based on the best cell-type signatures and cell classes from Moffitt *et al.* The colors of the cell classes top annotation correspond to the cell-type legend in Fig. 4B. The colors of the cell types are available in Supplementary Fig. 16; (B) A tSNE map of cell-type signatures with distinct expression. Cell-type clusters are visualized as a 2D t-SNE embedding of filtered local maxima vectors. Cell-type annotation and coloring are based on the best correlating segmentation-based cell-type signature from Moffitt *et al.* The tSNE map clearly shows the distinct cluster of different inhibitory and excitatory cell-type signatures. Cell types are grouped into classes based on groupings by Moffitt *et al.*; (C) The SSAM *de novo* 3D cell-type map showing spatial organization of the cell types signatures in the gene expression vector field. Below left and right a zoom in of the highlighted tissue regions of the ventricle structure and clusters of oligodendrocyte cell types. The colors of the cell types correspond to the cell-type legend in Fig. 4B; (D) Spatial localization of various inhibitory cell-type signatures. We found a number of inhibitory cell types which both matched expression signature and tissue localization described by Moffitt *et al.* See also Supplementary Fig. 22; (E) As panel D, but for excitatory cell types.

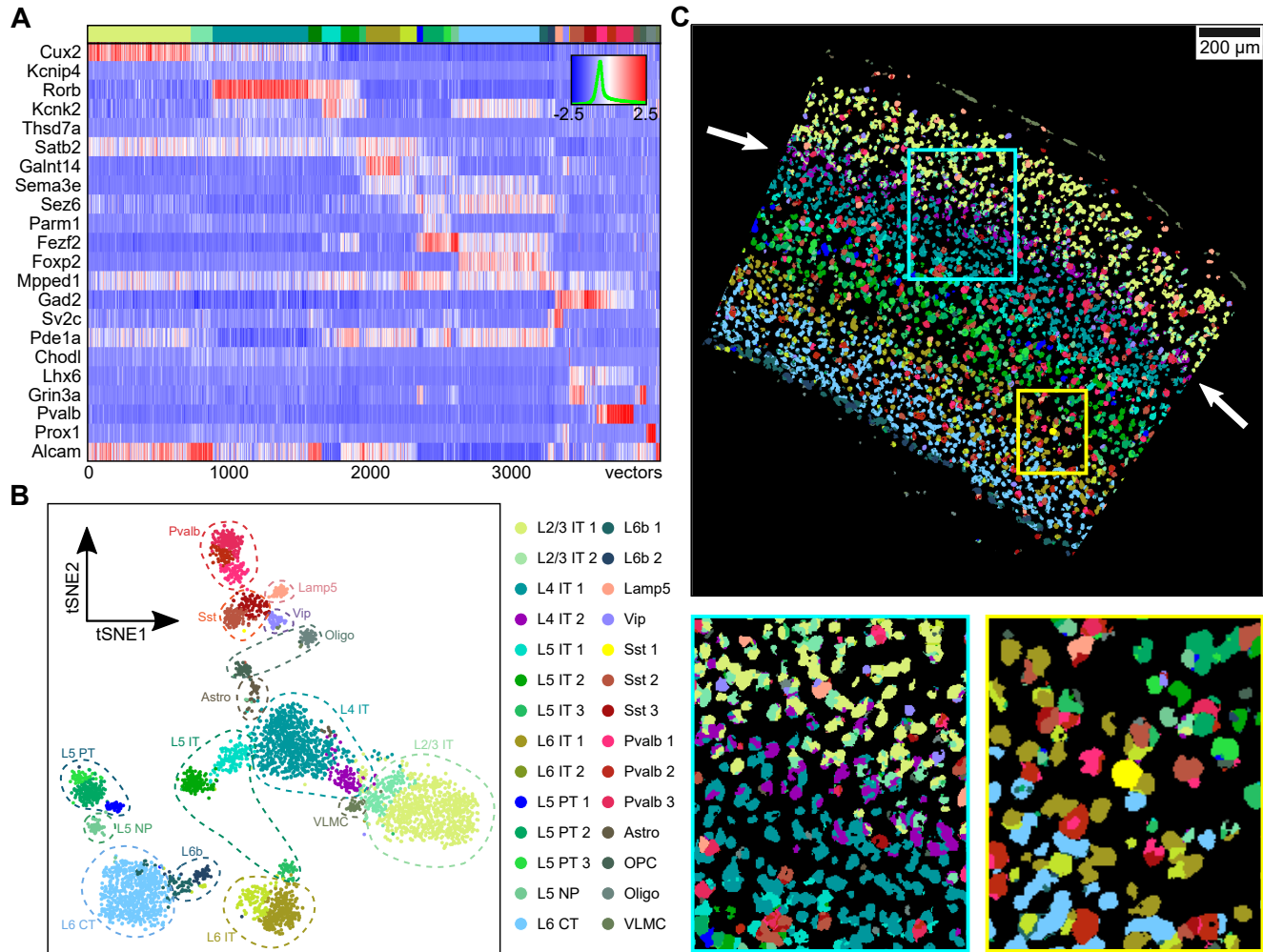


Figure 5. SSAM identifies layer structure in VISp and confirms rare Sst Chodl cell type in the mouse VISp region.

(A) Gene expression heatmap showing cell-type specific expression of marker genes (4,113 vectors). Rows show z-score normalized gene expression and columns show the gene expression patterns of filtered local maxima vectors. The top annotation shows the cell types and coloring based on the highest correlating single cell RNA-seq based cell-type signature from previous result (Tasic *et al.*, 2018). The colors of the top annotation correspond to the cell-type legend in Fig. 5B; (B) A tSNE map of cell-type signatures with distinct expression. Cell-type clusters are visualized as a 2D t-SNE embedding of filtered local maxima vectors, with groupings based on the supplementary table 9 of Tasic *et al.* 2018. Cell-type annotation and coloring are based on the best correlating segmentation-based cell-type signature from previous result (Tasic *et al.*, 2018); (C) The SSAM *de novo* cell-type map showing spatial organization of the cell types. Highlighted are the tissue regions of the cortex including novel L4 IT cell type sub-layering (main panel, purple, white arrows, lower left panel, see also Supplementary Fig. 29B), and rare Sst Chodl cell type (lower right panel, yellow, see also Supplementary Fig. 29C). The colors of the cell types correspond to the cell-type legend in Fig. 5B.

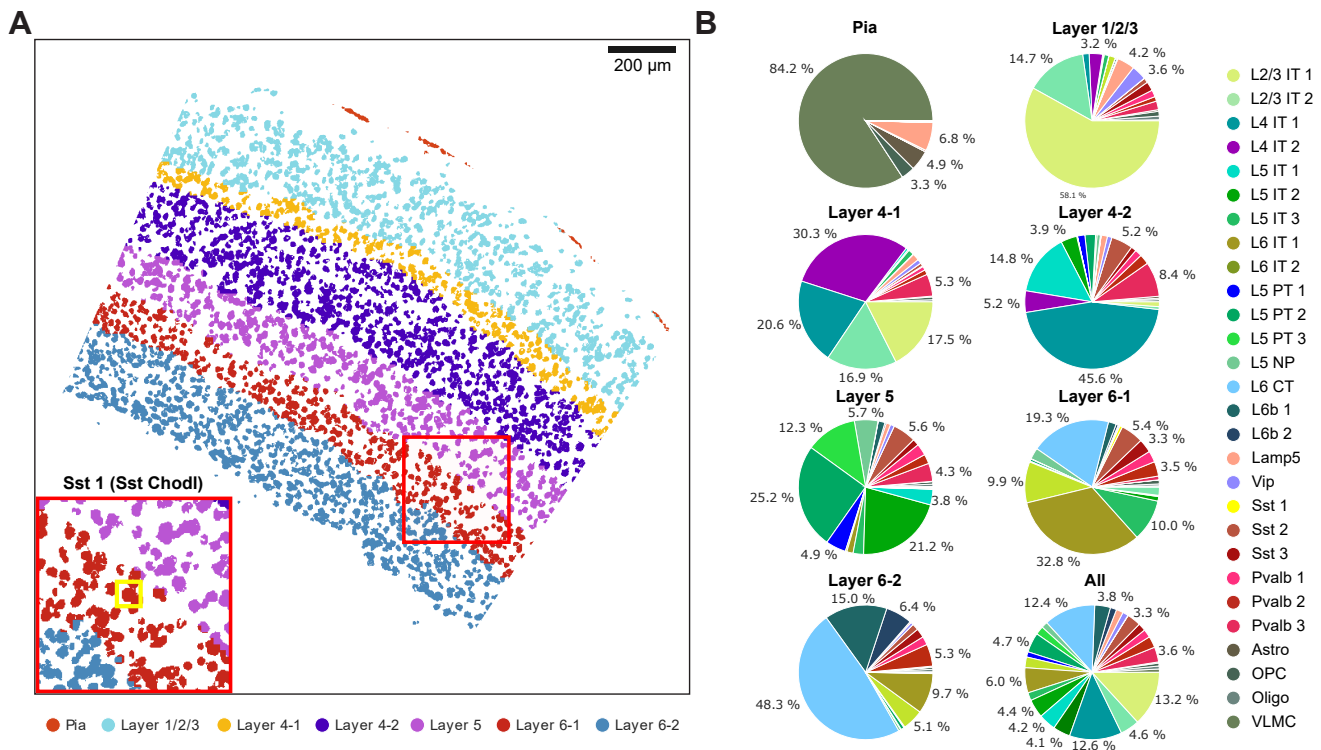


Figure 6. Rare Sst Chodl cell type localizes to the L6-1 layer of the mouse VISp region.

(A) Tissue domain map generated by SSAM. Tissue domain signatures were identified from clustering local cell-type composition over sliding 100 μ m circular windows, and projected back onto the cell-type map. The reconstruction shows the various cortical layers within the adult mouse VISp, with very clear separation of the Pia layer, and separation of layer 4 and layer 6 into 2 sub-layers. Inset zooms into the location of the rare Sst Chodl cell type found in layer 6-1; (B) Cell-type composition within each tissue domain.